JOURNAL OF AIRCRAFT
Vol. 53, No. 3, May-June 2016

Performance of a Mach-Scale Coaxial Counter-Rotating Rotor in Hover

Christopher G. Cameron,* Anand Karpatne,* and Jayant Sirohi†
University of Texas at Austin, Austin, Texas 78712

DOI: 10.2514/1.C033442

A Mach-scale rotor system, 2.03 m in diameter, was built and hover tested in three configurations: two-bladed single rotor, four-bladed single rotor, and two-bladed coaxial counter-rotating rotor. The blades were untwisted with a VR-12 airfoil profile and a constant chord of 76.2 mm with a 3.8 mm trailing-edge tab. The hubs were rigid and had a vertical spacing of 13.8% rotor radius. Individual rotor steady and vibratory hub loads as well as lower-rotor push-rod loads were measured for several blade loadings up to 0.095. Mean loads were used to analyze rotor performance with an analytical momentum theory model as well as to validate an in-house, free-vortex wake model. Statistical analysis of the measured data revealed clear trends with a known confidence level. Because of mutual interference, the upper and lower rotors of the coaxial configuration consumed 18 and 49% more induced power than that of an isolated two-bladed rotor. The coaxial counter-rotating configuration was found to consume 6% less induced power than an isolated four-bladed single rotor of equal solidity. While torque-balanced, the upper rotor was found to produce 54% of the total system thrust regardless of blade loading. Rotor performance was not affected with an unbalanced torque of up to 5%. The free-vortex wake model was used to gain insight into the flow physics responsible for the interference effects by exploring the radial inflow and thrust distributions.

Nomenclature

A	=	πR^2, disk area
C_D	=	airfoil sectional drag coefficient
C_P	=	$P/\rho A(\Omega R)^3 R$, power coefficient
C_T	=	$T/\rho A(\Omega R)^2$, thrust coefficient
F_P	=	push-rod force, positive upward
F_Z	=	load cell force in the vertical direction, positive upward
N	=	total number of vortex filaments in wake model
N_b	=	number of blades
R	=	rotor radius
T	=	thrust (single rotor: F_Z, upper rotor: F_{ZU}, lower rotor: $F_{\mathrm{ZL}} - \Sigma_{i=1}^{N_b} F_{P_i}$)
Γ	=	blade-bound circulation distribution
ζ	=	wake age, deg
λ	=	inflow velocity normalized by blade tip speed ΩR
ρ	=	air density
σ	=	$N_b c/(\pi R)$, rotor solidity (total solidity for coaxial rotor)
τ	=	$[C_{\mathrm{TL}} - C_{\mathrm{TU}}]/[C_{\mathrm{TL}} + C_{\mathrm{TU}}]$, rotor torque balance
ψ	=	rotor azimuth angle relative to upper- and lower-rotor blade crossing
Ω	=	rotor angular velocity

Subscripts

L	=	lower rotor in coaxial configuration
U	=	upper rotor in coaxial configuration

Superscript

$\hat{}$	=	estimated parameter

Received 11 March 2015; revision received 2 September 2015; accepted for publication 6 October 2015; published online 3 March 2016.

*Graduate Research Assistant, Department of Aerospace Engineering and Engineering Mechanics.

†Associate Professor, Department of Aerospace Engineering and Engineering Mechanics.

I. Introduction

THE substantial increases in forward-flight speed, range, and payload capacity demanded of next-generation helicopters are driving research and development of unconventional rotorcraft configurations. The compound helicopter configuration featuring a rigid, coaxial, counter-rotating (CCR) rotor system has been shown to meet these new requirements, and design concepts are being developed by several companies. The most notable of these recent designs resulted in a prototype, the Sikorsky X2 Technology Demonstrator, which achieved 250 kt level flight in 2010 [1]. The design of these advanced helicopters requires reliable and proven analytical tools of varying fidelities. Detailed experimental data, such as those gathered in the NASA/U.S. Army UH-60 airloads program [2], have been key in refining and validating analytical tools used for single-rotor design. In contrast, there is a noticeable absence of detailed experimental data for rigid, coaxial, counter-rotating rotors. The comprehensive review of 20th century coaxial-rotor research by Coleman [3] indicated a limited number of experimental data sets on coaxial rotors. Early research efforts on rigid, CCR rotor systems coincided with the development of the Sikorsky XH-59A demonstrator (Advancing Blade Concept) helicopter in the late 1960s [4]. Some data are available from tests related to this program, including reduced-scale (2-ft-diam) rotor tests [4], Froude-scaled aircraft tests [5] focusing on control aspects, and full-scale aircraft hover [6] as well as forward-flight tests [7]. The full-scale XH-59A hover data have seen limited use in correlation with computational work because comparison of these results to isolated rotor studies requires empirical corrections for fuselage interference.

Harrington [8] performed hover tests on two full-scale coaxial rotors. Both rotors were two-bladed, 25 ft in diameter with untwisted blades. The first rotor was tapered both in thickness and planform with a teetering hub and an interrotor spacing of 18.6% radius. The second rotor was tapered only in thickness with a rigid hub and spacing of 16% radius. In both cases, the maximum tip speed was limited to 500 ft/s. Subsequently, Dingeldein [9] performed more measurements on the first of these rotors in hover and in forward flight and compared the performance to that of a tandem rotor. Nagashima et al. [10] carried out experiments on a 0.76-m-diam rotor system. Individual upper- and lower-rotor loads were acquired over a range of rotor spacings at a tip speed of 120 m/s. The data were correlated with subsequent analytical and numerical studies [11] examining the interactional effects between upper and lower rotors. McAlister and Tung performed hover testing on the 48.9-in.-diam, 1/7-scale Army Aeroflightdynamics Directorate (AFDD) coaxial-

rotor system [12]. Tests were performed with isolated and coaxial rotors at various spacings and heights above ground. Results included steady thrust and torque measurements as well as flow characterization through PIV. Later work by Ramasamy [13] on the same system included comparisons of coaxial, tandem, and equivalent isolated rotor performance. However, these studies were limited to a tip Mach number of 0.23 and low blade loadings for the equivalent isolated rotor performance.

Despite the age and low tip speed of the Harrington experiments [8], this data set remains a benchmark for validation of modern comprehensive analyses as well as computational fluid dynamics (CFD) codes. For example, Lim et al. [14] used a comprehensive aeromechanics code (CAMRAD-II), including a free-vortex wake aerodynamic model to satisfactorily correlate the hover performance (mean thrust and torque) measured in the aforementioned coaxial-rotor tests (the Harrington rotor, the full-scale XH-59A, and the model-scale AFDD rotor). Lakshminarayan and Baeder [15] used a compressible Reynolds-averaged Navier–Stokes solver to predict the performance and unsteady loading of a CCR rotor system; the performance data from the Harrington experiments were used for validation.

The goal of this paper is to describe the performance of a Mach-scale, rigid CCR rotor in hover. A set of detailed experiments were conducted on a 2.03-m-diam CCR rotor system, including isolated two-bladed single-rotor tests, isolated four-bladed single-rotor tests, and two-bladed CCR rotor tests. Note that the flap frequency of the current rotor system is similar to that of a hingeless rotor, although the term "rigid" is used to make a distinction between the current rotor system that has no flap hinges and an articulated or hingeless rotor. A free-vortex wake analysis was developed and validated with the experimental measurements; this analysis was used to explore the interaction of the upper and lower rotors in the CCR system. Induced power, profile power, and spanwise inflow and thrust distributions were calculated using the analysis, and comparisons were made between the isolated single-rotor and coaxial-rotor behavior. A preliminary investigation of azimuthal thrust variation was also undertaken, although an in-place dynamic calibration of the load cells remains to be performed. Therefore, these results are not discussed in the present paper. In addition to aerodynamic measurements, blade stiffness distributions are reported to enable validation of these data with numerical models. Uncertainties and scatter in the measurements often make it difficult to discern different trends in closely spaced experimental data. Therefore, a statistical analysis has been included to enable comparisons of trends from different configurations at a known confidence level, for example, the single-rotor and coaxial-rotor systems.

II. Experimental Setup

A. Test Facility and Transmission

The experiments were performed at an indoor whirl tower facility measuring $50 \times 33 \times 60$ ft tall. The test facility consists of a hydraulic power unit, a support tower, a transmission, and a control room. The coaxial-rotor system is built around a belt-driven transmission assembly (shown in Fig. 1) and is powered by a single 100 hp hydraulic pump and motor system. A serpentine belt arrangement with an idler pulley reverses the lower-rotor rotation direction, whereas toothed belts ensure that both upper and lower rotors remain synchronized. The transmission is mounted on a support column that places the lower rotor 14.2 ft above the ground plane.

Fixed-frame instrumentation includes a $\pm 5g$ microelectromechanical systems accelerometer (Analog Devices ADXL-206) as well as bearing temperature monitors. A Hall-effect sensor mounted on the lower-rotor shaft generates a 1/rev signal used for synchronous averaging. Rotating frame measurements are passed through a 24-channel upper-rotor slip ring and a 26-channel lower-rotor slip ring.

B. Loads Measurement

1. *Rotating Frame Load Cells*

Hub loads are measured by two custom modified six-axis load cells (ATI Omega-160) [16]. The load cells feature onboard signal conditioning, ensuring that only high-level voltage signals are passed through the slip rings. Each load cell is supplied with two static calibrations covering varying load ranges. The resolution of thrust and torque measurements is 0.75 N and 0.025 N · m respectively, with bias accuracy of ± 7.5 N and ± 0.48 N · m. The high-gain silicon strain gauges allow for a very stiff construction, with isolated load cell natural frequencies greater than 1000 Hz in all directions. A fully coupled dynamic calibration of the load cells installed in the test setup is planned for the future.

2. *Push-Rod Loads*

The data discussed in this paper were acquired in two separate sets of tests performed six months apart featuring different pitch control systems. The first set of these tests was performed with manual individual blade pitch control and no swashplates. The upper-rotor pitch-adjustment system was designed with female rod ends on captive lead screws that react the pitching moment loads through the hub. With no load path in parallel to the rotating frame load cell, the need to measure and correct for upper-rotor push-rod loads was eliminated. The lower rotor employed turnbuckle based push rods that were not reacted through the hub. As a consequence, the push-rod loads were measured and compensated for in the lower-rotor force measurements. These push-rod loads were measured using full-bridge, strain-gauge instrumented flexure beams. Miniature strain-gauge signal conditioners (RAEtech 1169-01-50-100) were used to send amplified

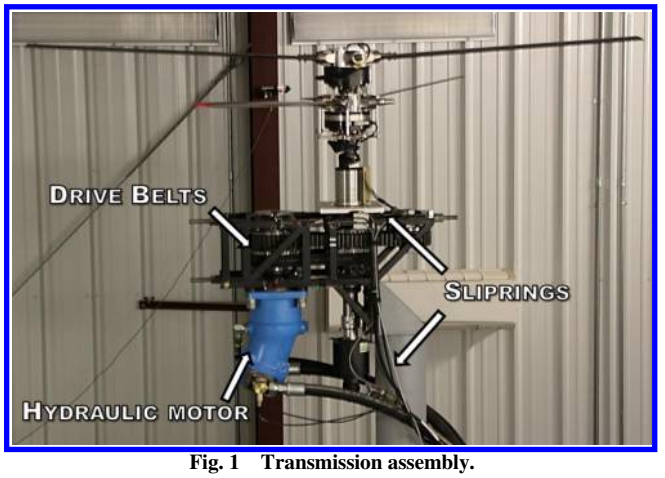

Fig. 1 Transmission assembly.

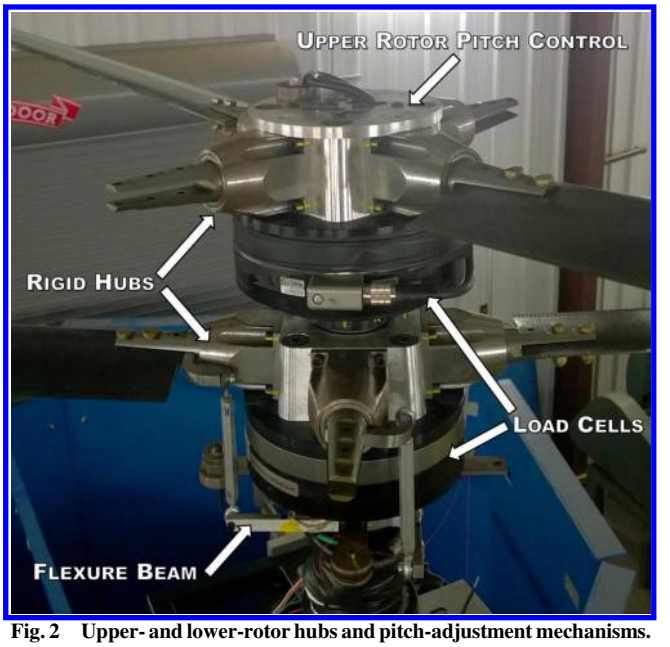

Fig. 2 Upper- and lower-rotor hubs and pitch-adjustment mechanisms.

signals through the slip ring. The flexure beams were calibrated by hanging weights from the push-rod mounting points and were found to resolve push-rod loads of less than 0.5 N. Upper- and lower-rotor hubs and pitch-adjustment mechanisms are shown in Fig. 2.

For the second set of tests, blade pitch was adjusted using two servo-actuated swashplate control assemblies, one for the upper rotor and another for the lower rotor. Push-rod loads were not measured during this second set of tests, and so the push-rod loads acquired in the first set of rotor tests was used to compensate the thrust measured in the second set of tests.

C. Data Acquisition

Data were acquired using a pair of National Instruments PXI-6358 simultaneous sampling, multifunction data acqusition cards at 30,000 samples per second with 16 bit resolution. High-speed counter inputs were used to acquire the 1/rev signal from the lower-rotor shaft, whereas each analog input was sent to a separate analog-to-digital converter. A LabVIEW virtual instrument (VI) was used to monitor all channels in real time for safety and troubleshooting. Synchronous averaging was triggered from the VI with raw data streamed to file for additional postprocessing.

D. Rotor System

The rotor system was designed and built in-house, with the goal of replicating the dynamic characteristics of a closely spaced, rigid rotor system such as on the X2 Technology Demonstrator helicopter [17]. A single two-bladed rotor, a single four-bladed rotor, and a coaxial counter-rotating rotor system with two blades in each rotor were tested. Parameters for all three tested configurations are listed in Table 1. An untwisted, untapered, constant section blade geometry was chosen both for ease of fabrication and to serve as a simple case for building a reference data set.

1. *Hubs and Pitch Control*

Similar to the X2 Technology Demonstrator, the hubs were designed without flap or lead-lag articulation. Each hub consists of a central support to which four modular bearing carrier assemblies attach. These carriers house hardened steel blade grips supported by roller bearings. An axial roller bearing supports centrifugal loading, whereas a pair of needle roller bearings react in- and out-of-plane forces including flap-bending and lead-lag moments. The hubs have 3 deg of precone built in to reduce stresses and deflections in the blades. The hubs are bolted to the six-component load cells, which are mounted directly on the rotor shafts.

As previously mentioned, no swashplate assemblies were used for the first set of hover tests. Collective pitch was set for each blade individually. The upper-rotor pitch control was designed to reside on the upper-rotor hub, eliminating the need to measure and compensate for push-rod loads in upper-rotor thrust measurements. The lower-rotor push rods were attached to a strain-gauge instrumented base attached below the load cell. For the second set of tests, two swashplate assemblies, one for each the upper and lower rotors, were used to adjust blade pitch.

Table 1 Summary of rotor properties

Property	Two-bladed single	Four-bladed single	Two-bladed coaxial
Interrotor spacing	— —	— —	0.140 m
Solidity (total rotor system)	0.050	0.100	0.100
Rotor radius	— —	1.016 m	— —
Root cutout (%R)	— —	12%	— —
Precone angle	— —	3 deg	— —
Airfoil section	— —	VR-12	— —
Chord	— —	0.080 m	— —
Tip speed	— —	153, 191 m/s	— —
Rotor speed, rpm	— —	1430, 1795	— —

2. *Blades*

The rotor blades were constructed using a thermoformed IG-31 foam core. A two-cell construction method was used with a forward D-spar created by wrapping the foam core with unidirectional IM7/3501-6 prepreg. Tungsten leading-edge weights and an aluminum root insert were secured in the D-spar using FM-300 film adhesive. The spar was then joined to the aft foam core, and the entire assembly was wrapped in a single layer of ±45 deg AS4/3501-6 prepreg. After curing in a female aluminum mold, the blades were finish-machined to their final dimensions.

Blade sectional stiffness properties (Table 2) were measured by clamping the blades at their root and applying tip loads. The values presented were calculated assuming uniform spanwise properties. A more detailed analysis using whole-field measurements of blade deformation in conjunction with nonuniform beam theory is planned. Blades 1 and 2 are upper-rotor blades, which were used in all three test configurations. Blades 3 and 4 are two additional upper-rotor blades used in the four-bladed isolated rotor testing, whereas blades 5 and 6 are the two lower-rotor blades.

III. Computational Method

The analysis was developed to validate experimental results and to explore the interactional aerodynamics between the two rotors in a coaxial-rotor system. In the past, a number of vortex-based techniques have been developed to model the aerodynamics of a single rotor. The "free-vortex method" (FVM) [18] involves discretizing the wake into small vortex filaments and then calculating the velocities induced by the filaments on each other. For wake evolution, either a relaxation-based approach or a time-marching approach can be used. The latter, being time accurate, can also be used to model transient flight conditions [19,20]. Additionally, the effects of vortex filament strain and viscous diffusion must be included for these models to accurately predict the core radius growth [21–23]. The FVM has also been extended to model a coaxial-rotor wake [3,24] by including the wake contribution of the second rotor. The current analysis is based on FVM and uses a time-accurate fourth order Runge–Kutta (RK4) explicit scheme for temporal advancement of the vortex filaments. This model was used to obtain performance estimates of a single and coaxial-rotor system, and the results were correlated with experiments.

A schematic of the rotor wake is shown in Fig. 3. The blade is discretized into several spanwise elements with a circulation distribution Γ_i. At each time step, as the rotor blade moves, wake elements are created adjacent to and in the plane of the rotor blade. The near wake consists of two parts: the trailed and shed wake. Trailed vorticity is caused due to a spanwise variation in the rotor blade circulation distribution ($d\Gamma/dx$), whereas the shed vorticity is caused due to the variations in the rotor blade circulation with time ($d\Gamma/dt$). After a specified period, the near wake is lumped into a concentrated tip and a root vortex. Each wake element induces velocities on one other, which is calculated using the Biot–Savart law. To compute the new blade-bound circulation, the total normal velocity computed at each blade spanwise station (control points located at 3/4th chord) is set to zero as shown in Eq. (1):

$$(\boldsymbol{V}_\infty + \boldsymbol{V}_{\mathrm{NW}} + \boldsymbol{V}_{\mathrm{FW}} + \boldsymbol{V}_{\mathrm{Blade}_i}) \cdot n_i = 0 \tag{1}$$

Here, $\hat{n}_i$ is the normal vector at the ith control point. $\boldsymbol{V}_\infty$ is the freestream velocity, $\boldsymbol{V}_{\mathrm{NW}}$ is the velocity induced due to the near wake,

Table 2 Blade sectional properties

Blade	Mass, g	Flap bending stiffness, N · m^2	Torsional stiffness, N · m^2
1	149.8	22.2	22.8
2	151.3	22.4	23.1
3	155.5	22.4	23.1
4	153.7	22.5	23.0
5	151.2	21.7	22.9
6	151.6	21.8	23.1

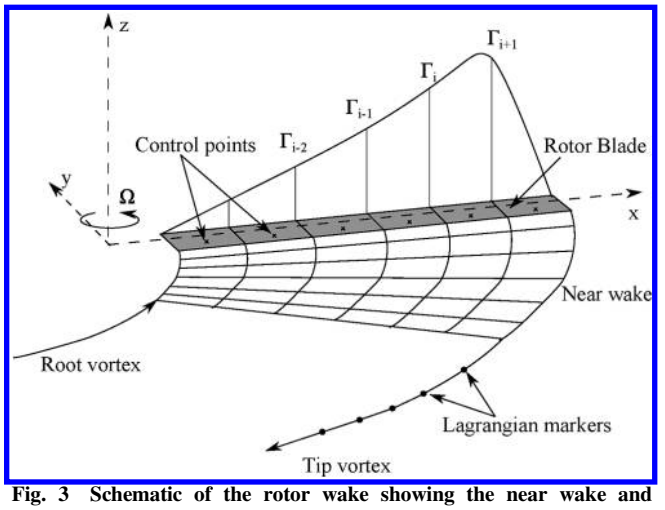

Fig. 3 Schematic of the rotor wake showing the near wake and concentrated tip and root vortices.

$\boldsymbol{V}_{\mathrm{FW}}$ is the velocity induced due to the concentrated tip vortex, and $\boldsymbol{V}_{\mathrm{Blade}_i}$ is the velocity induced by the blade-bound circulation at the control point. From this equation, the unknown values of Γ_i are obtained.

To compute the rotor thrust and power, the velocities induced by all the wake elements on the control points are obtained, and the effective induced angle of attack is calculated. A lookup table is then used to compute the values of lift and drag for every blade element. The two-dimensional (2-D) sectional airfoil lift/drag data for the VR-12 airfoil with a 5% tab was obtained using a 2-D, incompressible, steady-state simulation run in Fluent, at a Reynolds number of around 800,000, corresponding to the 3/4 radius location. Finally, the total thrust and drag are obtained by integrating elemental values of lift and drag over the blade.

A stable fourth-order RK4 scheme is used to study the evolution of the rotor wake as these vortex elements are convected in time with an azimuthal time step around 3–5 deg. The core radius of each cylindrical vortex element was modeled to include both viscous diffusion and filament strain effects as shown in Eq. (4):

$$\Delta r_{c,\mathrm{strain}} = r_c\left(1 - \frac{1}{\sqrt{1+\frac{\Delta l}{l}}}\right) \tag{2}$$

$$\Delta r_{c,\mathrm{diffusion}} = \sqrt{r_0^2 + 4\alpha_L \delta \nu \frac{\zeta}{\Omega}} - r_0 \tag{3}$$

$$r_c = r_0 + \Delta r_{c,\mathrm{strain}} + \Delta r_{c,\mathrm{diffusion}} \tag{4}$$

where r_c is the core radius of the vortex filament; l is the length of vortex filament; Δl is the change in filament length due to vortex stretching; $\alpha_L = 1.25643$ is Lamb's constant; δ is an experimental turbulent viscosity parameter as described by Bhagwat and Leishman [22]; ζ is the vortex age in degrees; and Ω is the rotational speed of the rotor. Furthermore, because the rotor tip speeds could be in the transonic regime, compressibility effects are modeled by including the Prandtl–Glauert factor in the Biot–Savart law for calculating induced velocities.

This methodology is extended to the case of a coaxial rotor by adding a second set of wake filaments representing the wake of the lower rotor. The interactions of the two sets of rotor wakes are obtained by calculating the mutually induced velocities between the two rotor wakes and the rotor blades. The net induced velocities on the rotor are then used to calculate the aerodynamic loads on each rotor. A torque trim condition is imposed at each time step by dynamically adjusting the upper-rotor blade pitch angles. The tolerance for torque trim condition is kept as 0.1% of the total rotor system torque, and simulations are run until mean torque and thrust converges.

This technique involves computing the effect of every vortex filament on every other filament. Therefore, the total computational cost involved in finding the induced velocities of all elements at each time step is on the order of $\mathcal{O}(N^2)$, if the rotor wake is approximated by N filaments, typically on the order of several thousands. Therefore, the total cost required to find velocities of all the elements of the wake is ($\mathcal{O}(N^3)$) operations. To improve computational efficiency, OPENMP was used for parallelizing the velocity computation subroutine such that the effect of a filament on another filament is independently computed on different cores. The time required to reach a torque-balanced steady-state solution for a prescribed lower-rotor collective was approximately 50 min running on two hex-core Xeon 5680 processors, representing speedup by a factor of 8.5 over a serial implementation.

IV. Experimental Procedure

In the first set of tests, data for each rotor configuration were acquired at five blade loadings. At each test condition, 100 revolutions of data were captured and phase averaged. Typical plots of phase-averaged thrust and push-rod loads for the lower coaxial rotor are shown in Fig. 4 at a tip speed of 190 m/s and $C_T/\sigma = 0.089$. In processing the performance data, the mean of each revolution is treated as a statistically independent sample. The mean and standard deviation of each of these 100 independent samples are then used to calculate the mean value and precision uncertainty of quantities at that test condition. For this first test, multiple runs were performed at each desired blade loading of the coaxial rotor, varying the torque balance between the upper and lower rotors. Torque balance τ is defined as the difference between upper- and lower-rotor torque normalized by total system torque as shown in Eq. (5):

$$\tau = \frac{(C_{\mathrm{QL}} - C_{\mathrm{QU}})}{(C_{\mathrm{QL}} + C_{\mathrm{QU}})} \tag{5}$$

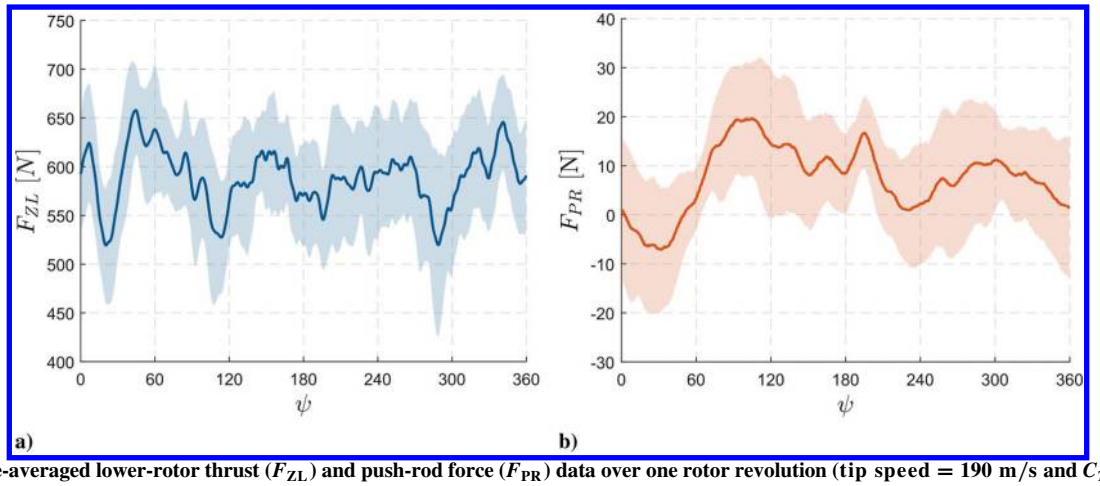

Fig. 4 Phase-averaged lower-rotor thrust (F_{ZL}) and push-rod force (F_{PR}) data over one rotor revolution (tip speed = 190 m/s and $C_T/\sigma = 0.089$).

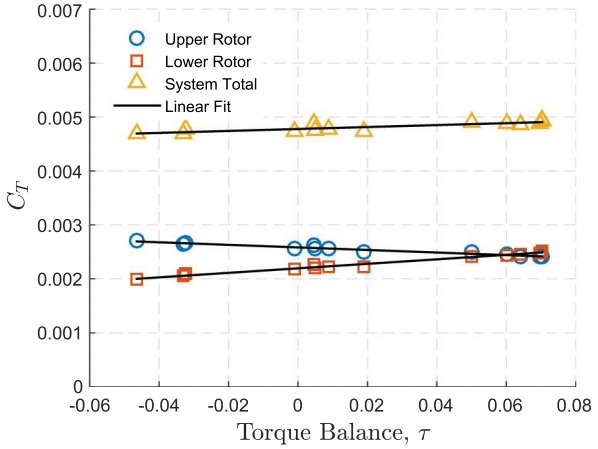

Fig. 5 Coaxial-rotor thrust vs torque balance τ with linear fits for estimating thrust at exactly torque-balanced condition.

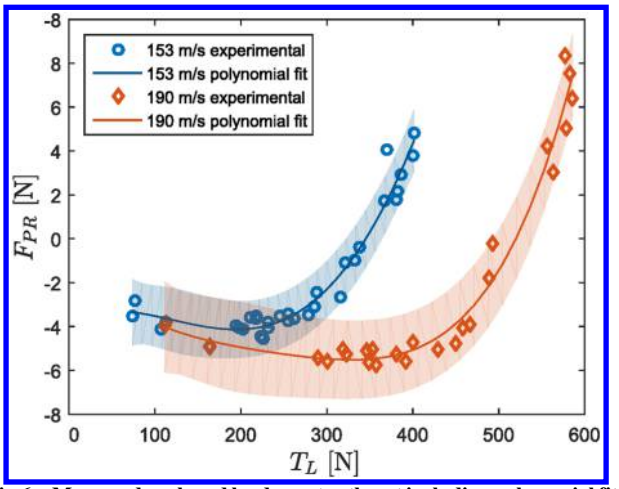

Fig.6 Measured push-rod load vs rotor thrust including polynomial fits with 95% confidence intervals.

Data were taken as near to torque-balanced as possible, which was found to occur at nearly equal upper and lower collectives. The torque balance was very sensitive to collective, with changes of approximately 0.25 deg collective resulting in up to a 10% change in torque balance. Because of this sensitivity, additional data were taken with small torque imbalances between upper and lower rotor at each blade loading. These data points, along with the nearly torque-balanced data, were then used to generate linear fits to interpolate the exactly torque-balanced condition, as well as ±5% unbalanced conditions. An example of raw data with overlaid linear fits is shown in Fig. 5.

For the second set of tests, the availability of servo-actuated swashplate controls simplified the trimming and data processing procedure. At each test condition, an upper-rotor collective pitch was set and the lower-rotor collective pitch adjusted until the system was as close to torque-balanced as possible. Postprocessing the second test data consisted of checking torque-balance values and discarding any points with $\tau > 0.03$. Because no push-rod forces were recorded during this second set of tests, quartic polynomials were fit to the mean push-rod forces from the first set of tests; these were used to compensate the thrust loads in the second set of tests. The measured push-rod forces, along with the polynomial fits and uncertainties used to compensate the second set of thrust data, are presented in Fig. 6. The interpolated push-rod force is multiplied by the number of push rods and subtracted from the measured thrust value. For the upper rotor, the push-rod forces are multiplied by an additional factor to account for the pitch-link geometry.

V. Statistical Analysis Techniques

The goal of the statistical analysis is to compare data from different experimental configurations and draw conclusions with a known confidence given the measurement uncertainties. The first step is to fit analytical models to the experimental data. In this paper, the models are restricted to linear fits of the form

$$y = \beta_1 x + \beta_0 \tag{6}$$

Then, statistical analysis is used to evaluate the regression coefficients of the analytical fits. For example, confidence intervals are calculated based on the distribution of measurements and the analytical fits. Student's t-test is used to compare two different sets of data in terms of the regression coefficients of their analytical fits. Detailed descriptions and derivations of the statistical analysis techniques can be found in the textbook by Ryan [25].

Shaded confidence intervals plotted with the analytical model provide a visual indication of the uncertainty of the estimates $\hat{y}_i$ for various values of x_i. A 95% confidence interval is defined such that, with repeated sampling, 95% of the generated confidence intervals are expected to contain the true value y_i. The expression for this confidence interval is given as Eq. (7):

$$P(\hat{y}_0 - \delta_y \le y_0 \ge \hat{y}_0 + \delta_y) = 0.95 \tag{7}$$

where, given a set of n measurements used to generate the analytical fit,

$$\delta_y = t_{0.025,n-2} S_\epsilon \sqrt{\frac{1}{n} + \frac{(x_0 - \bar{x})^2}{S_{xx}}} \tag{8}$$

$$S_\epsilon = \sqrt{\frac{\Sigma(y_i - \hat{y}_i)^2}{n-2}} \tag{9}$$

$$S_{xx} = \sum_{i=1}^{n} (x_i - \bar{x}_i)^2 \tag{10}$$

$t_{0.025,n-2}$ is the t-statistic calculated at the 95% confidence level for a Student's t-distribution with n-2 degrees of freedom (i.e., $\alpha = 0.95$), and the p-value is $(1-\alpha)/2 = 0.025$. In addition to these fit confidence intervals, the 95% confidence intervals for the coefficients of the analytical fits are calculated as follows:

$$P(\hat{\beta}_0 - \delta_{\beta 0} \le \beta_0 \ge \hat{\beta}_0 + \delta_{\beta 0}) = 0.95 \tag{11}$$

$$P(\hat{\beta}_1 - \delta_{\beta 1} \le \beta_1 \ge \hat{\beta}_1 + \delta_{\beta 1}) = 0.95 \tag{12}$$

$$\delta_{\beta 1} = t_{0.025,n-2} \sqrt{\frac{\Sigma_{i=1}^{n}(y_i - \hat{y}_i)^2}{(n-2)S_{xx}}} \tag{13}$$

$$\delta_{\beta 0} = t_{0.025,n-2} S_\epsilon \sqrt{\frac{\Sigma_{i=1}^{n} x^2}{n S_{xx}}} \tag{14}$$

For example, this approach is used to calculate the uncertainties in the induced power and profile power coefficients fit to the measured power using momentum theory.

With the analytical fit coefficients and their uncertainties, Student's t-test is then used to compare measurements from different experimental configurations. The null hypothesis for comparing coefficients from two fits, a and b, is that they are equal; the resulting t-statistic is calculated using the coefficients and their standard errors as

$$t = \frac{\hat{\beta}_{n,a} - \hat{\beta}_{n,b}}{\sqrt{s^2_{\hat{\beta}_{n,a}} + s^2_{\hat{\beta}_{n,b}}}} \tag{15}$$

A p-value is computed using this t-statistic and a t-distribution with $n-2$ degrees of freedom, where n is the lesser of the number of points used to create the two fits. This p-value is the probability of observing a test statistic at least as extreme as that calculated [from Eq. (15)]. If this p-value is greater than 0.025, the null hypothesis is accepted, which means that the coefficients are found to have no statistical difference with a confidence level of 95%. On the other hand, if this p-value is less than 0.025, the null hypothesis is rejected, in which case there is a significant difference between the coefficients and, consequently, between the two sets of measurements.

VI. Results and Discussion

A. Data Compilation

1. Tip-Speed Effect

During the first set of tests, data were collected at two different tip speeds, 153 and 190 m/s, corresponding to blade chord-based Reynolds numbers of 5.8×10^5 and 7.4×10^5 at the 3/4 span location. To compare the performance of the rotor systems, an analytical model derived from momentum theory, shown in Eq. (16), was fit to the measured data using a linear least-squares regression. In this Reynolds number regime, it is important to check for the impact of tip speed on the performance characteristics of the rotor, especially as related to the profile power, because the airfoil C_d is sensitive to the Reynolds number. The coaxial-rotor system performance data at both tip speeds is plotted in Fig. 7, and the induced power coefficient and profile power are given in Table 3 along with 95% confidence intervals. There is no statistical difference in induced power or profile power of the rotor system at the two tip speeds ($p = 0.349$ and $p = 0.387$, respectively). The two tip speeds are therefore combined in the following sections:

$$C_P/\sigma = \kappa\sqrt{\sigma}\frac{(C_T/\sigma)^{3/2}}{\sqrt{2}} + \frac{C_{P0}}{\sigma} \tag{16}$$

2. Different Test Setups

As previously described, a second set of tests were performed six months after the first set. In between tests, the rotor system was completely dismantled and reassembled with a new pitch control system. The two sets of test data were compared by the same methods used to compare the effect of tip speed; the results are shown in Fig. 8 and Table 3. The second set of tests was performed at lower blade loadings; as such, the extrapolated momentum theory model shows greater disagreement with the first set of tests at higher blade loadings. However, as in the case of the different tip speeds, there was no statistically significant difference in induced power or profile power between tests 1 and 2 ($p = 0.167$ and 0.325, respectively). This indicates good repeatability in the performance measurements, even separated by six months and with completely different pitch control systems.

Table 3 Rotor test performance comparison

Rotor system	Induced power coefficient κ	Profile power $C_{P0} \times 10^4$
Test 1 (tip speed = 150 m/s)	1.320 ± 0.034	1.511 ± 0.105
Test 1 (tip speed = 190 m/s)	1.330 ± 0.041	1.514 ± 0.132
Test 2	1.281/0.077	1.585/0.177

3. Effect of Torque Balance

The same linear fits used to interpolate an exactly torque-balanced condition in the test 1 data were also used to interpolate the performance of the rotor system with torque imbalances of $\tau = \pm 0.05$. These data are plotted along with the torque-balanced data in Fig. 9. Note that, because of the nature of the linear fits, there is increased uncertainty in the unbalanced performance curves. However, there is no statistically significant difference in rotor performance between the three conditions. This result is in agreement with the momentum theory derivations by Leishman and Syal [26] that showed a negligible change in induced power coefficient for a torque-balanced compared to that of a thrust-balanced rotor system, a similarly small change in torque balance. Further measurements targeting various torque-balance conditions could reduce the uncertainty of the unbalanced data as well as reveal trends in performance at higher imbalance ratios; however, the typical operating condition for a helicopter with a CCR rotor system is with the torque balanced (i.e., yaw trim condition).

B. Performance

First, both isolated rotor configurations were processed, and the thrust versus power curves were compared to the FVM predictions (Fig. 10). The experimental data are plotted with 95% confidence intervals based on the combination of the observed measurement precision and the load cell bias error. These data were used to verify the VR-12 lift and drag polars used in the FVM simulations. Good agreement is seen without any additional modification to the lookup tables calculated in Fluent. The simulations appear to slightly underpredict the measured power requirements for both the two- and four-bladed isolated rotors at higher thrust levels while falling within the uncertainty bounds. In Fig. 11, the FVM predictions are compared to the measured performance of the two-bladed coaxial rotor. It is clear that the FVM model is able to achieve good correlation to the experimental results across all investigated thrust values. Once again,

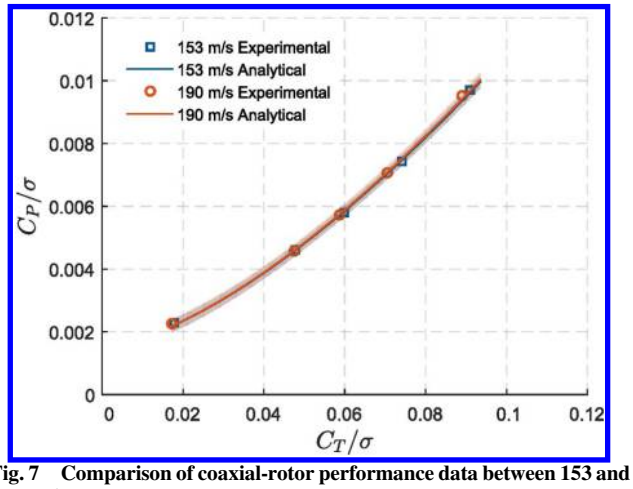

Fig. 7 Comparison of coaxial-rotor performance data between 153 and 190 m/s tip speeds.

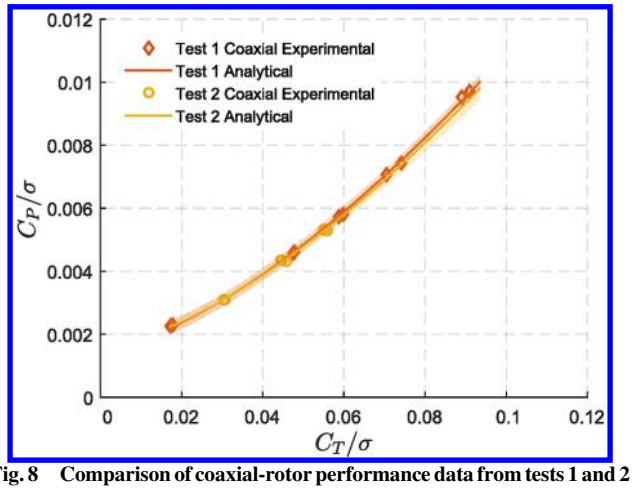

Fig. 8 Comparison of coaxial-rotor performance data from tests 1 and 2 conducted six months apart.

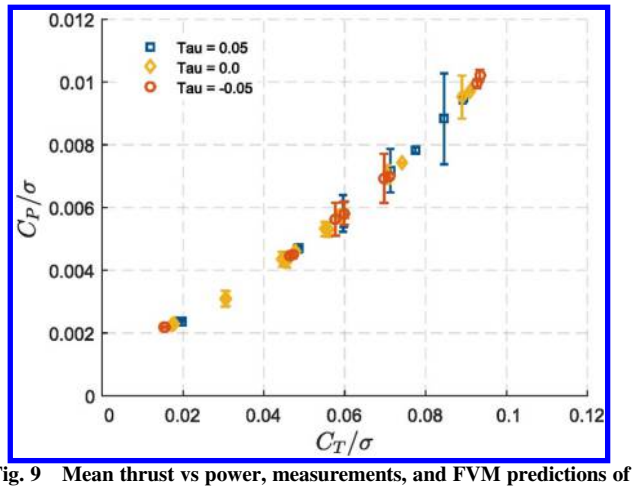

Fig. 9 Mean thrust vs power, measurements, and FVM predictions of single-rotor configurations.

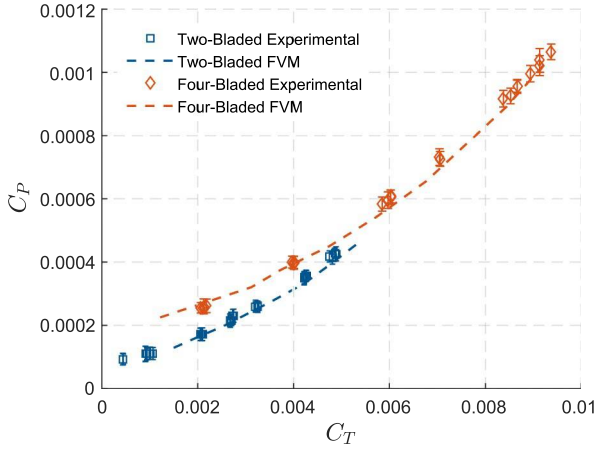

Fig. 10 Mean thrust vs power, measurements, and FVM predictions of single-rotor configurations.

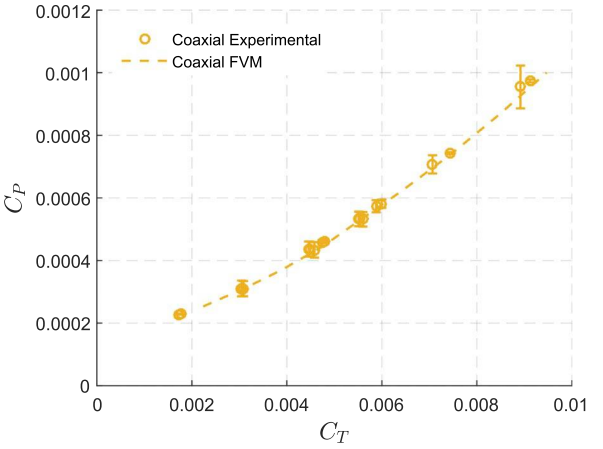

Fig. 11 Mean thrust vs power, measurement, and FVM prediction of the two-bladed coaxial-rotor system.

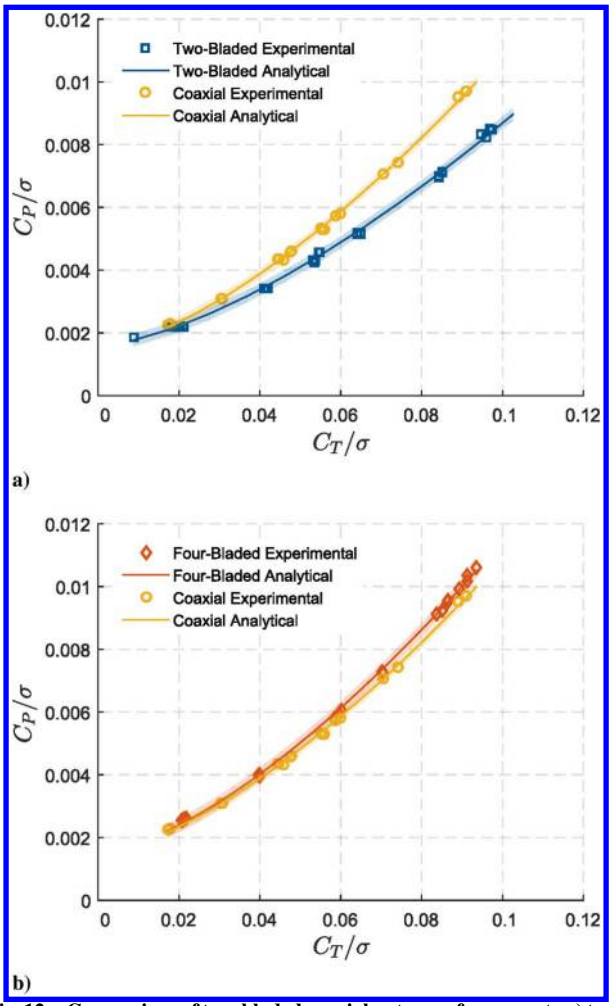

Fig. 12 Comparison of two-bladed coaxial-rotor performance to a) two-bladed single rotor, and b) four-bladed single rotor.

the analysis slightly underpredicts the power requirements at the highest thrust levels, but agreement is better at lower thrust levels than for the isolated rotors.

To compare the isolated rotor systems to the coaxial system, thrust versus power is plotted normalized by rotor solidity in Figs. 12a and 12b. Plotted with the experimental data are analytical momentum theory fits with shaded 95% confidence intervals; the coefficients of these fits are listed in Table 3. Figure 12a shows the two-bladed single rotor consuming significantly less power on a per-blade basis than the coaxial-rotor system at higher thrust values. This is due to the reduced solidity of the two-bladed isolated rotor affecting the per-blade induced power, as seen in the factor of $\sqrt{\sigma}$ multiplying the induced power term in Eq. (16). The two-bladed isolated rotor may consume less power per blade at a given blade loading but has an overall thrust capacity of approximately half the coaxial-rotor system. A better comparison is between systems that are geometrically identical in blade planform and solidity, differing only in rotor configuration. This is shown in Fig. 12b, where the coaxial-rotor system is compared to the isolated four-bladed rotor. Here, the two systems appear similar, with the coaxial rotor consuming slightly less power at higher blade loadings.

Table 4 shows the induced power coefficients and profile powers of the rotor systems with 95% confidence intervals calculated from the regression. The four-bladed isolated rotor and the two-bladed coaxial system, having equal solidity, show no statistical difference in profile power, whereas the difference in the induced power coefficient is significant with $p = 3.5 \times 10^{-4}$. The ratio of the two-bladed coaxial induced power coefficient to that of the four-bladed rotor system, referred to by Ramasamy [13] as a separation coefficient κ_{sep}, is 0.942 ± 0.022. This means that the coaxial-rotor system consumes 6% less induced power than the equivalent isolated rotor system. These measurements validate computational results reported by Kim and Brown [27] for the Harrington coaxial rotor and a notional equivalent four-bladed isolated rotor. Similar experimental results were obtained by Nagashima et al. [10], who found that a coaxial-rotor system consumed up to 6% less power than the equivalent solidity single rotor, as well as by Ramasamy [13], who showed a 10% decrease in induced power for an equivalent solidity coaxial rotor. The induced power coefficient of the two-bladed isolated rotor is slightly higher than that of the four-bladed rotor; however, the

Table 4 Rotor system performance comparison

Rotor system	Induced power coefficient κ	Profile power $C_{P0} \times 10^4$
Two-bladed isolated	1.419 ± 0.022	0.793 ± 0.028
Four-bladed isolated	1.406 ± 0.021	1.506 ± 0.087
Two-bladed coaxial	1.325 ± 0.023	1.513 ± 0.074
Two-bladed coaxial upper	1.672 ± 0.044	0.765 ± 0.056
Two-bladed coaxial lower	2.115 ± 0.029	0.753 ± 0.030

difference is not statistically significant. Additionally, the two-bladed isolated rotor exhibits approximately one-half the profile power of the four-bladed isolated and two-bladed coaxial rotors, a result expected from blade element momentum theory.

The FVM model is used to further explore the components of the rotor system power (Fig. 13). Here, there is a clear difference in induced power between the two-bladed isolated rotor and both the four-bladed isolated and two-bladed coaxial rotors. Indeed, the agreement between the rotor systems of equivalent solidity suggests that the difference in per-blade power with the two-bladed rotor system is simply due to a solidity effect. Note also that the predicted profile power remains nearly constant across all test conditions. This is important because it validates the usage of the momentum theory model in Eq. (16), which is derived assuming a constant profile power coefficient.

C. Upper and Lower Coaxial-Rotor Performance

Considering upper- and lower-rotor hub load data separately, the interactional effect on the performance of the upper and lower coaxial rotors are investigated by comparing each with an isolated two-bladed single rotor of equivalent solidity and planform. Figure 14 compares the performance of the upper and lower rotors with the data measured from the isolated two-bladed rotor. The upper- and lower-rotor performances are greatly impacted due to aerodynamic interaction resulting in increased power consumption. This behavior is well captured by the FVM model. The same analytical model used to fit overall rotor system performance is used for the individual rotors, as shown in Fig. 15 as well as in Table 4. A quantitative measurement of the interference effect is obtained by taking the ratio of the individual coaxial-rotor induced power factors to that of the isolated two-bladed rotor system. This quantity, referred to as the rotor-on-rotor influence factor by Ramasamy [13], is found to be $\kappa_U = 1.178 \pm 0.035$ and $\kappa_L = 1.490 \pm 0.030$ for the upper and lower rotors, respectively. The lower rotor suffers the greater performance impact with 49% increased induced power compared to an isolated two-bladed single rotor, whereas the upper rotor only shows 18% increase. The mean power increase of the system (33.4%) falls between momentum theory estimates of the induced power interference factor given by Leishman and Syal [26] as $\kappa_{\text{int}} = 1.414$ for coplanar rotors and $\kappa_{\text{int}} = 1.2818$ for a lower rotor operating in the fully developed slipstream of the upper rotor.

The relationship between upper- and lower-rotor thrust in the torque-balanced condition is explored further in Fig. 16a. Here, the thrusts are seen to follow linear trends of different slopes with increasing system thrust. Predictions from the FVM are overlaid and show excellent agreement with the experimental data. Figure 16b shows the ratio of upper rotor to total system thrust at both the balanced and unbalanced conditions. In the balanced configuration, the ratio is nearly constant, with the upper rotor producing $53.8 \pm 2.0\%$ of the total thrust. This result is consistent with the analysis

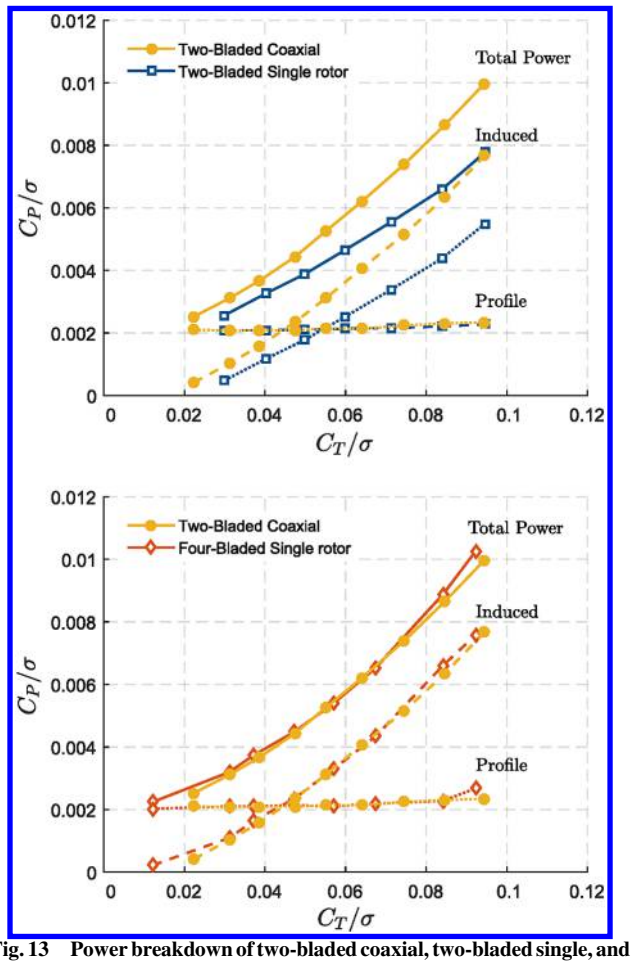

Fig. 13 Power breakdown of two-bladed coaxial, two-bladed single, and four-bladed single-rotor systems calculated using the FVM.

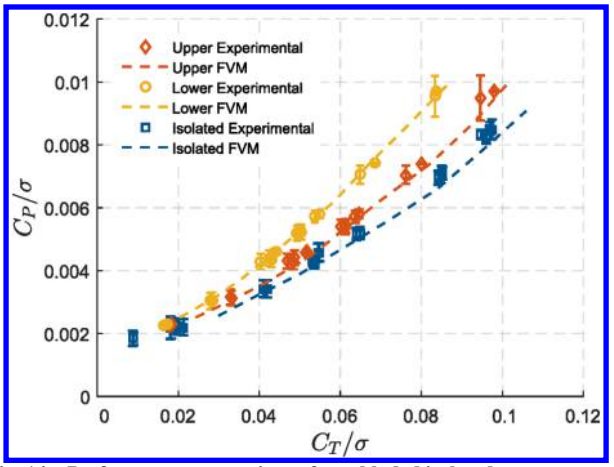

Fig. 14 Performance comparison of two-bladed isolated rotor to upper and lower coaxial rotors with FVM predictions.

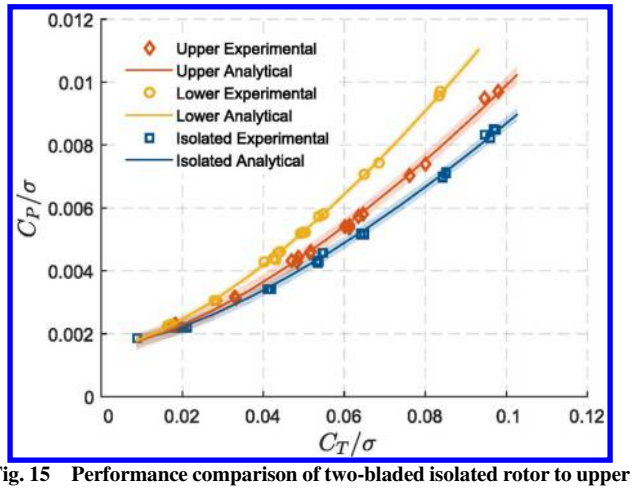

Fig. 15 Performance comparison of two-bladed isolated rotor to upper and lower coaxial rotors with analytical fit.

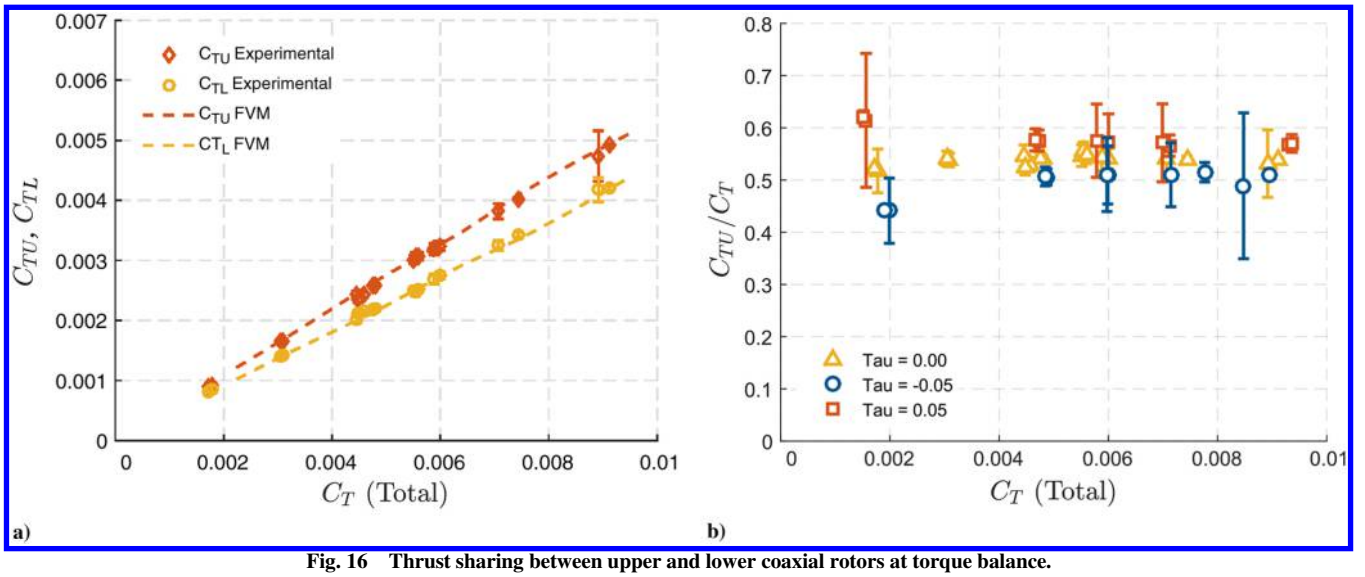

Fig. 16 Thrust sharing between upper and lower coaxial rotors at torque balance.

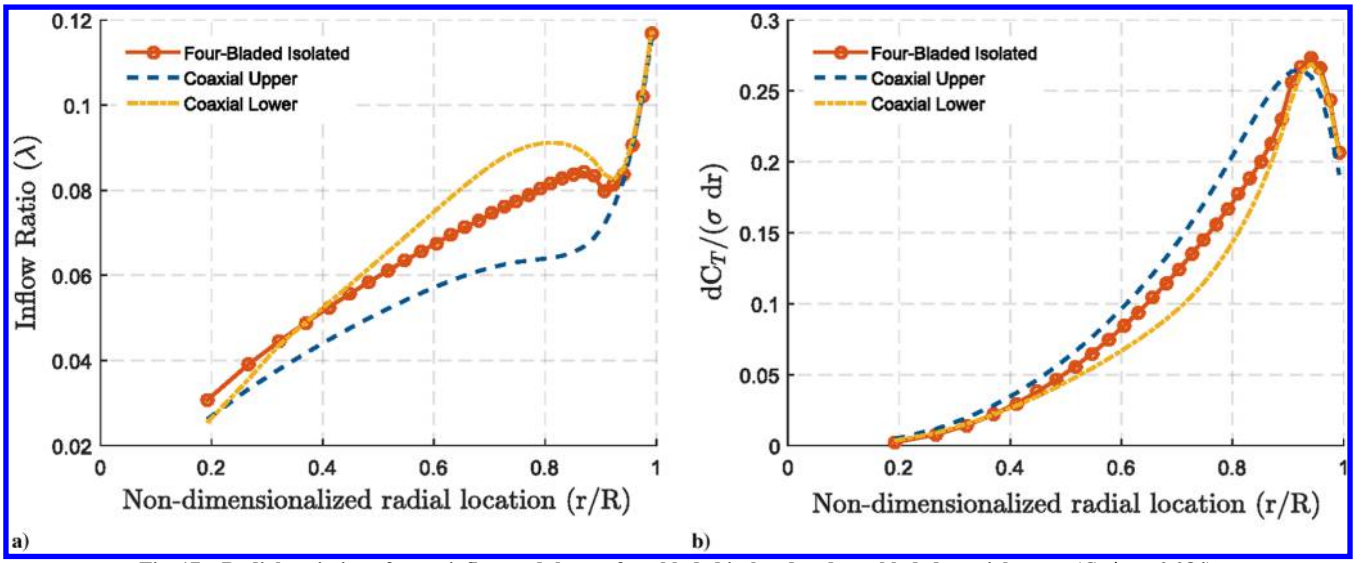

Fig. 17 Radial variation of rotor inflow and thrust: four-bladed isolated and two-bladed coaxial rotors ($C_T/\sigma = 0.084$).

performed on the Harrington rotor data by Kim and Brown [27], the experimental and analytical results of Nagashima et al. [10], and the experimental work of Ramasamy [28]. Although the uncertainty in the torque unbalanced conditions is significant, the mean thrust ratios are calculated as 49.4 ± 6.4 and $58.1 \pm 4.4\%$ for the $\tau = 0.05$ and $\tau = -0.05$ cases. Note that the -5% torque unbalance case nearly achieves an equal thrust condition for the upper and lower rotors.

The computations from the FVM also give an estimate of the radial variation of rotor inflow and thrust production as shown in Fig. 17. In Fig. 17a, the inflow ratio λ is plotted against radial location for both the four-bladed isolated rotor as well as the upper and lower coaxial rotors. There is a significant increase in lower-rotor inflow due to the upper-rotor wake, and upper- and lower-rotor inflow conditions straddle the four-bladed isolated rotor inflow, especially farther from the blade root. This phenomenon, with the four-bladed rotor distribution falling between the upper- and lower-rotor distributions, is seen again in Fig. 17b, where the blade thrust distribution is plotted against the radial location. These results agree with the findings of Kim and Brown for the Harrington rotor system [29]. Overall, aerodynamic interference effects cause the increase in upper- and lower-rotor induced power consumption when compared to the isolated two-bladed rotor and, when averaged, result in a total system performance similar to the isolated four-bladed rotor.

VII. Conclusions

A Mach-scale, rigid, counter-rotating coaxial-rotor system, 2.032 m in diameter and operating at tip speeds of 153 and 190 m/s, was built and hover tested. Three configurations were investigated: two-bladed single rotor, four-bladed single rotor, and two-bladed counter-rotating coaxial rotor up to a maximum blade loading (C_T/σ) of approximately 0.095. Hub loads and lower-rotor pitch-link loads were recorded along with a 1/rev signal for synchronous averaging. Rotor performance was found to be statistically similar at the chosen tip speeds as well as across two tests conducted six months apart, demonstrating measurement repeatability.

Performance measurements for both the isolated and the coaxial-rotor systems showed good agreement with a free-vortex wake analysis without any modification of the CFD computed airfoil tables. A momentum theory model was fit to the experimental data to compare profile and induced powers. Comparisons between the four-bladed isolated and two-bladed coaxial rotors revealed a statistically significant difference (with 95% confidence) in induced power, with the coaxial rotor consuming 6% less power than the isolated rotor. This result is significant because the coaxial-rotor system outperforms the equivalent single-rotor system without taking into account additional realizable efficiency gains such as the lack of necessity for a tail rotor.

The wake interactions between the upper and lower rotor were clearly visible in the individual rotor performance. The analytical model revealed 18 and 49% increases in induced power for the upper and lower coaxial rotors when compared to an equivalent isolated two-bladed rotor. The interactions were also seen in the radial variation of inflow and thrust as computed by the FVM analysis. Thrust sharing between upper- and lower-rotor coaxial rotors with the system torque-balanced was found to be nearly constant, with the upper rotor providing 54% of the total thrust at all collectives. These results were also in close agreement with the free-vortex method predictions.

Future work will involve a detailed dynamic calibration of the hub-mounted load cells, so that the vibratory forces can be quantitatively compared to analytical predictions. The rotor systems will be tested in the Glen L. Martin wind tunnel in forward flight examining the effect of lift offset on coaxial-rotor system efficiency. Finally, push-rod loads will be analyzed and correlated with analysis as well as vibratory hub loads.

Acknowledgments

The work presented was supported by the U.S. Army, U.S. Navy, and NASA Vertical Lift Research Center of Excellence program, Task A-1.4, as well as Army Research Office grant W911NF1310463. The composite materials for blade construction were donated by Bell Helicopter. The authors thank undergraduate research assistant Jesse Dearden for his expertise and assistance in building the rotor blades as well as machinist Joseph Pokluda for the numerous parts fabricated for the rotor system.

References

[1] Bagai, A., "Aerodynamic Design of the X2 Technology Demonstrator Main Rotor Blade," *Proceedings of the American Helicopter Society 64th Annual Forum* [CD-ROM], AHS International, Alexandria, VA, April–May 2008.

[2] Kufeld, R., Balough, D. L., Cross, J. L., Studebaker, K. F., Jennison, C. D., and Bousman, W. G., "Flight Testing of the UH-60A Airloads Aircraft," *Proceedings of the American Helicopter Society 50th Annual Forum* [CD-ROM], AHS International, Alexandria, VA, May 1994.

[3] Coleman, C. P., "A Survey of Theoretical and Experimental Coaxial Rotor Aerodynamic Research," NASA TP-3675, 1997.

[4] Cheney, M., "The ABC Helicopter," *Journal of the American Helicopter Society*, Vol. 14, No. 4, 1969, pp. 10–19. doi:10.4050/JAHS.14.10

[5] Phelps, A. E., and Mineck, R. E., "Aerodynamic Characteristics of a Counter-Rotating, Coaxial, Hingeless Rotor Helicopter Model with Auxiliary Propulsion," NASA TM-78705, May 1978.

[6] Arents, D. N., "An Assessment of the Hover Performance of the XH-59A Advancing Blade Concept Demonstration Helicopter," U.S. Army Air Mobility Research and Development Lab., TR USAAMRDL-TN-25, Fort Eustis, VA, May 1977.

[7] Felker, F. F., "Performance and Loads Data from a Wind Tunnel Test of a Full-Scale, Coaxial, Hingeless Rotor Helicopter," NASA TM-81329, Oct. 1981.

[8] Harrington, R. D., "Full-Scale-Tunnel Investigation of the Static-Thrust Performance of a Coaxial Helicopter Rotor," NASA TN-2318, 1951.

[9] Dingeldein, R. C., "Wind-Tunnel Studies of the Performance of Multirotor Configurations," NACA TN-3236, Aug. 1954.

[10] Nagashima, T., Ouchu, H., and Sasaki, F., "Optimum Performance and Load Sharing of Coaxial Rotor in Hover," *Journal of Japan Society for Aeronautics and Space Sciences*, Vol. 26, No. 293, June 1978, pp. 325–333. doi:10.2322/jjsass1969.26.325

[11] Nagashima, T., and Nakanishi, K., "Optimum Performance and Wake Geometry of a Coaxial Rotor in Hover," *Vertica*, Vol. 7, Nos. 225–239, 1983, pp. 225–239.

[12] McAlister, K. W., and Tung, C., "Experimental Study of a Hovering Coaxial Rotor with Highly Twisted Blades," *Proceedings of the American Helicopter Society 64th Annual Forum* [CD-ROM], AHS International, Alexandria, VA, April–May 2008.

[13] Ramasamy, M., "Hover Performance Measurements Toward Understanding Aerodynamic Interference in Coaxial, Tandem, and Tilt Rotors," *Journal of the American Helicopter Society*, Vol. 60, No. 3, 2015, Paper 032005. doi:10.4050/JAHS.60.032005

[14] Lim, J. W., McAlister, K. W., and Johnson, W., "Hover Performance Correlation for Full-Scale and Model-Scale Coaxial Rotors," *Journal of the American Helicopter Society*, Vol. 54, No. 3, 2009, Paper 32005. doi:10.4050/JAHS.54.032005

[15] Lakshminarayan, V. K., and Baeder, J. D., "High-Resolution Computational Investigation of Trimmed Coaxial Rotor Aerodynamics in Hover," *Journal of the American Helicopter Society*, Vol. 54, No. 4, 2009, Paper 042008. doi:10.4050/JAHS.54.042008

[16] "Six Axis Force/Torque Sensor System Installation and Operation Manual," ATI Industrial Automation, Apex, NC, April 2012.

[17] Blackwell, R., and Millott, T., "Dynamics Design Characteristics of the Sikorsky X2 Technology™ Demonstrator Aircraft," *Proceedings of the American Helicopter Society 64th Annual Forum* [CD-ROM], AHS International, Alexandria, VA, April–May 2008.

[18] Bagai, A., and Leishman, J. G., "Rotor Free-Wake Modeling Using a Pseudo-Implicit Technique-Including Comparisons with Experimental Data," *Journal of the American Helicopter Society*, Vol. 40, No. 3, 1995, pp. 29–41. doi:10.4050/JAHS.40.29

[19] Bhagwat, M. J., and Leishman, J. G., "Stability, Consistency and Convergence of Time-Marching Free-Vortex Rotor Wake Algorithms," *Journal of the American Helicopter Society*, Vol. 46, No. 1, 2001, pp. 59–71. doi:10.4050/JAHS.46.59

[20] Bhagwat, M. J., and Leishman, J. G., "Rotor Aerodynamics During Maneuvering Flight Using a Time-Accurate Free-Vortex Wake," *Journal of the American Helicopter Society*, Vol. 48, No. 3, 2003, pp. 143–158. doi:10.4050/JAHS.48.143

[21] Ramasamy, M., and Leishman, J. G., "The Interdependence of Straining and Viscous Diffusion Effects on Vorticity in Rotor Flow Fields," *Proceedings of the American Helicopter Society 59th Annual Forum* [CD-ROM], AHS International, Alexandria, VA, May 2003.

[22] Bhagwat, M. J., and Leishman, J. G., "Generalized Viscous Vortex Core Models for Application to Free-Vortex Wake and Aeroacoustic Calculations," *Proceedings of the 58th Annual Forum of the American Helicopter Society* [CD-ROM], AHS International, Alexandria, VA, 2002.

[23] Young, L. A., "Vortex Core Size in the Rotor Near-Wake," NASA TM-2003-212275, 2003.

[24] Bagai, A., and Leishman, J. G., "Free-Wake Analysis of Tandem, Tilt-Rotor and Coaxial Rotor Configurations," *Journal of the American Helicopter Society*, Vol. 41, No. 3, 1996, pp. 196–207. doi:10.4050/JAHS.41.196

[25] Ryan, T. P., *Modern Regression Methods*, 2nd ed., Wiley, Hoboken, NJ, 2009, pp. 17–25.

[26] Leishman, J. G., and Syal, M., "Figure of Merit Definition for Coaxial Rotors," *Journal of the American Helicopter Society*, Vol. 53, No. 3, 2008, pp. 290–300. doi:10.4050/JAHS.53.290

[27] Kim, H. W., and Brown, R. E., "A Rational Approach to Comparing the Performance of Coaxial and Conventional Rotors," *Journal of the American Helicopter Society*, Vol. 55, No. 1, 2010, Paper 12003. doi:10.4050/JAHS.55.012003

[28] Ramasamy, M., "Measurements Comparing Hover Performance of Single, Coaxial, Tandem, and Tilt-Rotor Configurations," *Proceedings of the American Helicopter Society 69th Annual Forum* [CD-ROM], AHS International, Alexandria, VA, May 2013.

[29] Kim, H. W., and Brown, R. E., "A Comparison of Coaxial and Conventional Rotor Performance," *Journal of the American Helicopter Society*, Vol. 55, No. 1, 2010, Paper 012004. doi:10.4050/JAHS.55.012004